Fuel 232 (2018) 833–844

Contents lists available at ScienceDirect

Fuel

journal homepage: www.elsevier.com/locate/fuel

Full Length Article

3D CFD simulation of a CI engine converted to SI natural gas operation using the G-equation

Jinlong Liu, Cosmin E. Dumitrescu*

West Virginia University, 275 Eng. Sci. Bldg., Morgantown, WV 26505, USA

ARTICLE INFO

Keywords:
3D CFD simulation
G-equation
RANS
Spark-ignition
Natural gas
Re-entrant bowl

ABSTRACT

The conversion of heavy-duty CI engines to natural gas (NG) SI operation have the potential to increase the use of NG in the transportation sector in the United States. More, the increased turbulence of a bowl-in-piston combustion chamber can increase the flame speed under more efficient lean conditions. The main objective of this study was to investigate if a 3D G-equation-based RANS simulation (i.e., reasonable computational costs and running times) can predict the efficiency and emissions of such converted engine, for various NG compositions and operating conditions. The model was validated with experimental data from a single-cylinder CI research engine that replaced the fuel injector with a spark plug and fumigated NG inside the intake manifold using a low-pressure gas injector. Using a unique set of model tuning parameters, the model was able to qualitatively predict the effect of NG composition on engine performance and emissions over a range of operating conditions that changed spark timing, equivalence ratio, and engine speed. The model also captured the double-peak heat release rate seen at advanced spark timing in the experiments. The results showed that a lower methane number (MN) increased peak pressure and indicated mean effective pressure. Higher H/C ratio advanced combustion phasing. More, higher MN lowered nitrogen oxides but increased unburned hydrocarbons emissions. However, while a lower MN increased carbon monoxide (CO) production during the combustion process, there was no clear trend for engine-out CO emissions. Overall, the predicted gas composition effects on engine efficiency and emissions were relatively small, at least for the range of operating conditions investigated here. However, the results suggest that the 3D CFD model described here is suitable for combustion phenomena analysis such the flame behavior in a bowl-in-piston combustion chamber.

1. Introduction

Forecasts predict that the internal combustion (IC) engine will continue to be the main power source in the transportation sector for the foreseeable future [1]. As a result, increased use of alternative fuels such as natural gas (NG) for on- and off-road vehicles can reduce the dependence on petroleum-based fuels and curtail engine-out emissions [2]. In addition to abundant resources in North America, NG's higher hydrogen-to-carbon (H/C) ratio reduces engine-out CO_2 emissions compared to conventional fuels, hence lower greenhouse gas emissions [3].

Conventional spark ignition (SI) engines can be easily retrofitted to NG operation [4]. The downside is a lower volumetric efficiency that decreases the engine power output compared to gasoline [5,6]. But NG SI engines can run leaner than their gasoline counterparts, which reduces the pumping work [7]. Furthermore, leaner operation not only decreases engine-out carbon monoxide (CO) and unburned hydrocarbon (HC) emissions, but also lowers nitrogen oxides (NO_x) emissions due to a lower combustion temperature [1,3,8,9]. Meanwhile, leaner operation increases the thermal efficiency by decreasing the heat transfer and increasing the combustion efficiency. The disadvantage of the lean combustion is a slower flame propagation speed, which can result in flame extinction before completely consuming the fuel-air mixture [7,10]. However, NG's higher octane-number compared to gasoline allows an increase in the engine compression ratio, which would increase both the flame speed and engine efficiency. This suggests that NG would be a good candidate to replace diesel in compression-ignition (CI) engines. But NG has a higher auto-ignition temperature compared to diesel fuel, which makes it difficult to control the engine operation without additional modifications [7]. A solution is for NG to only partially replace the diesel fuel, which will still initiate and control the combustion process [7]. However, this approach requires two fuel tanks and dual NG-diesel controls, which can greatly increase the engine cost [11]. Another solution is to convert the CI engine to SI operation by replacing the fuel injector with a spark plug that would ignite the fuel-air mixture [1,3,7,9]. NG is then fumigated inside the

* Corresponding author at: MAE Dept., West Virginia University, P.O. Box 6106, Morgantown, WV 26506, USA.
E-mail address: cosmin.dumitrescu@mail.wvu.edu (C.E. Dumitrescu).

https://doi.org/10.1016/j.fuel.2018.05.159
Received 15 March 2018; Received in revised form 27 May 2018; Accepted 29 May 2018
Available online 28 June 2018

Nomenclature and Abbreviations

AHRR	Apparent Heat Release Rate
ATDC	After Top Dead Center
BTDC	Before Top Dead Center
CAx	CAD Corresponding to x % Mass Fraction Burned
CAD	Crank Angle Degree
DOC	Combustion Duration
DPIK	Discrete Particle Ignition Kernel
EVO	Exhaust Valve Opening
IMEP	Indicated Mean Effective Pressure
IVC	Intake Valve Closing
MFB	Mass Fraction Burned
RANS	Reynolds Averaged Navier-Stokes
SOC	Start of Combustion
ST	Spark Timing
TDC	Top Dead Center

intake manifold using a gas injector or injected directly inside the combustion chamber. The use of a hot surface is an alternative to using a spark plug (hence the name "hot ignition") for direct-injected NG engines, but it is not easily controllable at all operating conditions [7]. It is important to note that regardless of the retrofitting solution, appropriate engine calibrations are needed to control the high rate of pressure rise specific to premixed NG combustion and avoid knocking, especially at medium and high load conditions. This study investigates the more economical solution of replacing the fuel injector with a spark plug and the addition of a low-pressure gas injector in the intake manifold. This approach requires the least amount of engine modifications and/or calibrations, which is important for increased NG utilization. In addition, one of the cylinders can be used to compress the natural gas for applications that only have access to low-pressure NG gas lines (i.e., no access to CNG stations). However, the lack of information in the literature, particularly the information on the fundamentals of the combustion process in retrofitted single-fuel NG CI engines, can create difficulties in designing the controlling architecture for these engines.

Most of the literature that investigated fundamental NG combustion used experimental setups not representative of engine geometry (e.g., constant-volume vessels or rapid-compression machines) [1,9,12]. More, a major focus was on evaluating the efficiency of existing aftertreatment systems on the emissions of vehicles equipped with such retrofitted CI engines [13,14]. Further, numerous experimental investigations were focused on dual-fuel strategies, hence the large number of dual-fuel CFD simulations in the literature compared to CI engines converted to SI NG operation. Donateo et al. [15,16] built a model with suitable combustion chamber shape and engine control parameters from the database of different bowl-in-piston combustion chambers. This model then evaluated the performance and knocking tendency of DI engines converted to NG SI operation. Jiao et al. [17] and Yin et al. [18] used NG SI models to investigate the temperature and gas velocity distributions, and the overall turbulent kinetic energy inside bowl-in-piston chambers, which are different from the conventional roof-type combustion chamber in a gasoline engine. Adding to the combustion chamber geometry effects, NG composition varies with geographical source, time of year, and the treatments applied during production and/or transportation [3,7]. For example, in addition to (mostly) methane (CH_4), NG also contains heavier hydrocarbons (ethane, propane, butane, etc.) and inert diluents (N_2 or CO_2), which can significantly affect engine performance and emissions [19,20]. As a result, the engine control unit (ECU) must be capable of adjusting the engine operation to variations in NG composition [7]. All these issues suggest a need for both experimental and CFD work that not only investigate premixed combustion mode in a bowl-in-piston geometry (i.e., a diesel-like environment), but also the effects of NG detailed composition, if the economical retrofitting solution mentioned above is to be adopted.

The main objective of this study was to create a 3D numerical simulation of a heavy-duty CI engine converted to SI NG operation. The model was based on experimental data from a single-cylinder CI research engine that replaced the fuel injector with a spark plug and fumigated NG inside the intake manifold using a low-pressure gas injector. The goal was to build a tool capable of predicting the NG combustion behavior in a diesel environment (i.e., bowl-in-piston) that requires reasonable computational resources and/or running time. Of particular interest were predictions of NG composition effects on in-cylinder flame propagation and on the overall engine performance.

2. Experimental setup

The experiments were conducted in a single-cylinder research engine (Ricardo/Cussons, U.K., Model Proteus), which is based on a commercial heavy-duty diesel engine (Volvo, Sweden, Model TD120). Table 1 shows engine specifications and Fig. 1 shows the engine setup. The original diesel injector was replaced by a NG spark plug (Stitt, USA, Model S-RSGN40XLBEX8.4-2) and NG was delivered using a gas injector (Rail Spa, Italy, Model IG7 Navajo, 3 seats). A piezo-electric pressure transducer (Kistler, Model 6011) was installed in the glow plug location and connected to a charge amplifier (Kistler, Model 5010) to measure in-cylinder pressure. An aftermarket engine management system (Megasquirt, Model 3X) controlled engine operation conditions such as gas injection, spark timing (ST) and duration. In-house-built data acquisition software (Scimitar) collected operating data such as engine speed, torque, air, coolant, and oil temperature, and air mass flow. Ref. [3] details the engine setup.

The engine oil and coolant temperatures were maintained constant throughout the experiments. Steady-state engine experiments were conducted at several operating conditions that changed ST from −10 to −30 CAD ATDC, equivalence ratio from 0.71 to 0.80 for methane and from 0.69 to 0.76 for natural gas, and engine speed from 900 rpm to 1300 rpm [3]. Table 2 details the gas chemical composition.

3. 3D CFD simulation

Compared to a conventional SI engine (i.e., roof-type head), the combustion chamber geometry of the engine modeled in this work (i.e., bowl-in piston) changes the combustion behavior (i.e., the flame propagation) [9]. More, the experimental data (that will be discussed later) showed two heat-release peaks for advanced ST, which is not usually observed in conventional SI engines. As a result, a 3D CFD IC engine

Table 1
Engine specifications.

Engine manufacturer and model	Ricardo/Cussons, Proteus
Research engine type	Single-cylinder
Cycle	4-stroke SI PFI
Valves per cylinder	2
Bore [mm] x Stoke [mm]	130.2 × 150
Displacement [liters]	1.997
Intake valve open	12 CAD BTDC exhaust
Intake valve close	140 CAD BTDC compression
Exhaust valve open	126 CAD ATDC compression
Exhaust valve close	10 CAD ATDC exhaust
Connecting rod length [mm]	275
Squish height [mm]	2
Geometric compression ratio	13.3:1
Combustion chamber	Bowl-in piston

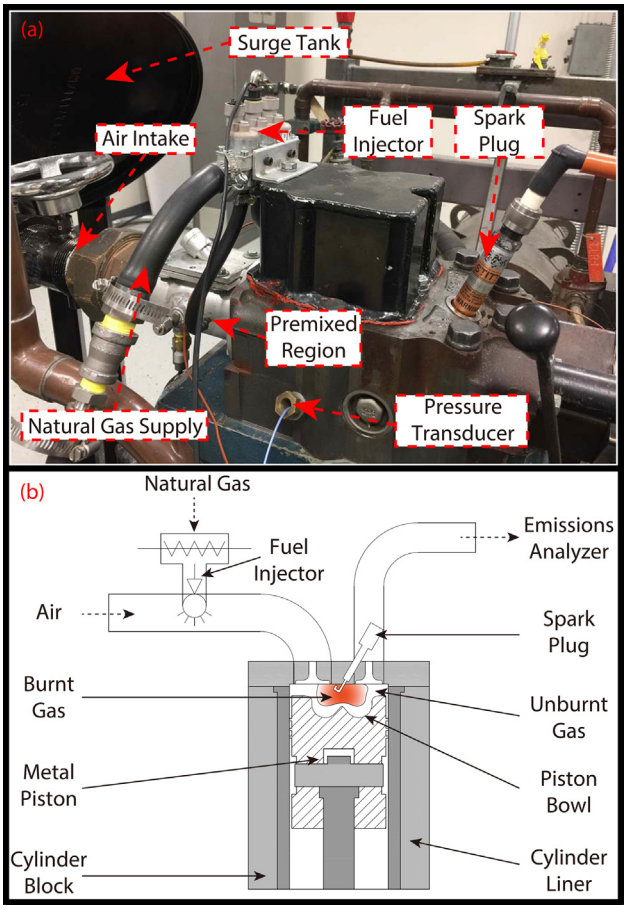

Fig. 1. Engine setup.

Table 2
Gas compositions.

Composition	Methane	Natural Gas
Methane	99.5%	90.909%
Ethane	0.1%	5.81%
Propane	–	2.39%
Butane	–	0.45%
Iso-butane	–	0.421%
Nitrogen	0.4%	0.02%
Total	100%	100%

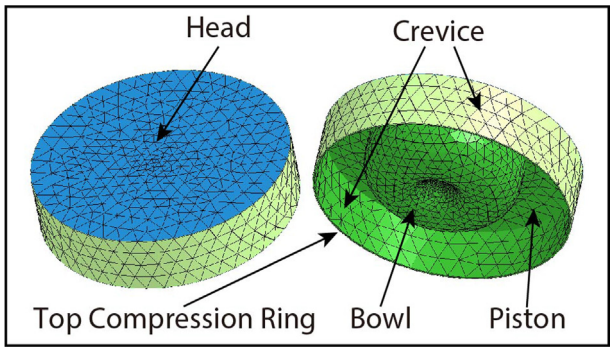

Fig. 2. Engine model mesh geometry.

software (ANSYS® Forte, Version 17.2) was used to predict engine performance of the CI engine converted to NG SI operation.

The simulation used the software's built-in NG mechanism that

Table 3
Natural gas properties.

Gas	Gas-1	Gas-2	Gas-3	Gas-4	Gas-5
CH_4	82.3%	90.8%	88.4%	95.9%	92.5%
C_2H_6	12.9%	5.2%	7.5%	0.1%	3.1%
C_3H_8	0.1%	2.6%	0.0%	2.6%	0.0%
CO_2	2.2%	0.1%	4.0%	0.7%	4.1%
N_2	2.5%	1.3%	0.1%	0.7%	0.3%
MN	80	85	90	95	100
H/C ratio	3.76	3.81	3.85	3.90	3.94

Table 4
Simulated operating conditions. The bold italics denote the baseline condition.

Spark timing [CAD ATDC]	−30, −25, −20, −15, ***−10***
Equivalence ratio [–]	***0.8***, 0.9, 1.0
Engine speed [rpm]	900, ***1300***, 1700, 2100

consists of 39 species and 268 reactions. This mechanism was reduced from a larger kinetics mechanism consisting of ~4000 species and validated for a range of equivalence ratios (0.4–2), pressure (1–100 bar), temperatures (1200 K and higher), and EGR (0–20%) [21]. The n- and iso-butane shown in Table 2 for the real gas composition were not included in the CFD gas because the above chemical mechanism does not include these two components. In addition, their concentration was negligible compared to the other gas components. A discrete particle ignition kernel flame (DPIK) model [22–24] simulated the kernel inception using Lagrangian particles and considering a kernel flame smaller than the mesh size. A turbulent combustion model, the G-equation [25,26], tracked the development of the turbulent flame front location. Chemistry is calculated outside of the flame, in the unburned and burned regions, and it is decoupled from the turbulent flame propagation. While such approach can influence the results accuracy compared to a fully coupled turbulence-combustion model, the G-equation can provide acceptable and faster results for any analysis that use a large number of simulations such as the study of NG composition effects using multiple gas combinations under multiple engine operating conditions. Compared to a truly predictive model, the G-equation model predicts in-cylinder turbulent flame combustion without including chemistry source terms in the transport equations [27]. The local turbulent flame speed used by G-equation was extrapolated from ANSYS® Forte's built-in library of laminar flame speeds that includes methane, ethane, and propane. Specifically, the software calculated the adiabatic, premixed, laminar flame speed over a range of equivalence ratios (0.3–2), pressures (10–90 bar), unburned gas temperatures (500–1000 K), and EGR rates (0–40%) using detailed (high-temperature) kinetics [21]. Next, the laminar flame speed was extrapolated to local conditions by sampling points within the table calculated at the previous step using a linear-least-square fit of a power law/Gulder equation. Consequently, the G-equations, the Reynolds-Averaged Navier Stokes (RANS) equations, and the Re-normalized group (RNG) k-ε model (turbulence model) [28,29] constitute a closed set of equations that completely describe the turbulent flame propagation [30,31]. The resulting flame front information is then used to calculate in-cylinder heat release, end gas kinetics, and emissions formation [25]. The simulation also included flame quenching and wall heat transfer models.

The 3D model did not simulate the intake and exhaust flow due to the large computational cost associated to it. Fig. 2 shows the combustion chamber model and mesh (cylinder head, cylinder liner, and piston) at the top dead center (TDC). A full 360° mesh was used due to the off-axis position of the bowl-in-piston. The spark plug was located on the bowl center axis. More, the model included a crevice volume off the side of the piston. The size of this crevice was adjusted to match the geometric compression ratio because other crevice regions such as the valve crevices, valve recesses etc. were neglected. The squish height

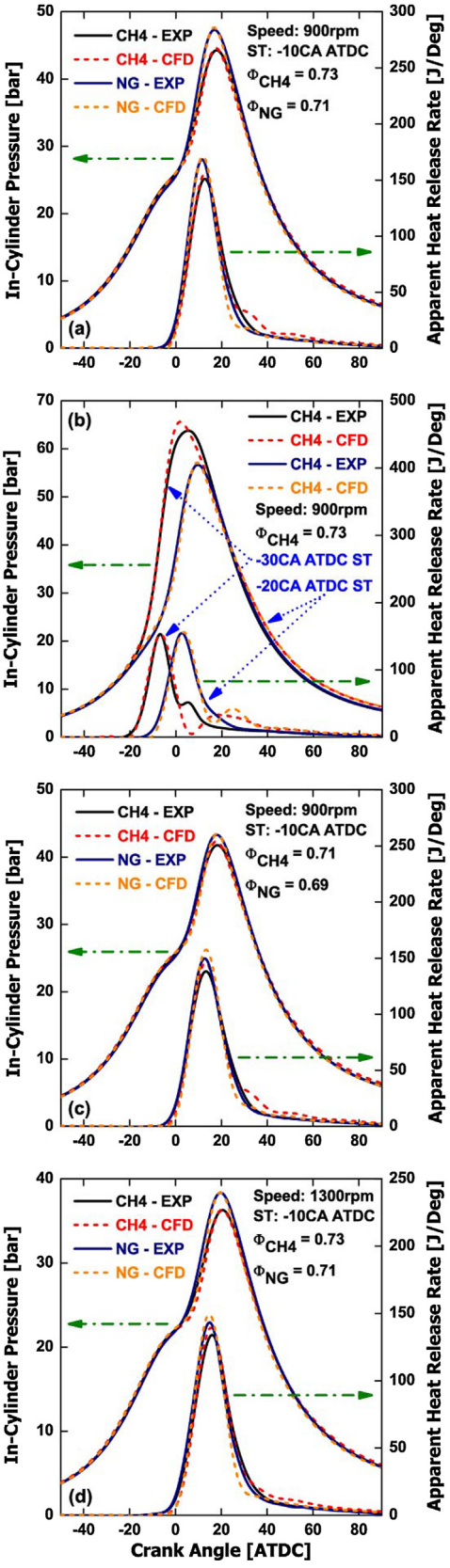

Fig. 3. In-cylinder pressure and AHRR at (a) baseline condition, (b) several spark timings (methane only), (c) several equivalence ratios, and (d) several engine speeds.

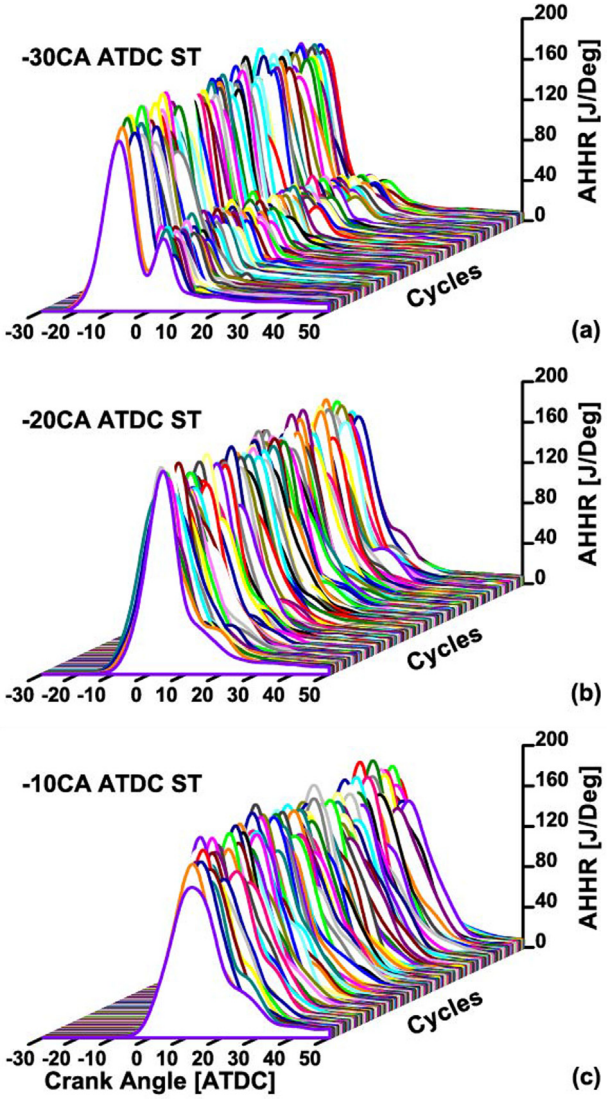

Fig. 4. Effect of spark timing on the apparent heat release rate of individual engine cycles.

was kept close to the one in the real engine to reasonably match in-cylinder flow phenomena after the intake valve closing (IVC).

The simulation started from IVC and completed at exhaust valve opening (EVO), assuming a homogeneous mixture of NG, air, and residual gas (2% of the exhaust mass). A counter-clockwise swirl motion was added at IVC (initial swirl ratio of 1.0 and initial swirl profile factor of 3.11 [32]) to simulate the intake-generated swirl in the real engine. The simulation applied uniformly-distributed and constant boundary temperature. In addition, the simulation used automatic mesh-generation at each piston position based on defined mesh-size criteria and specified mesh refinement controls. For example, the global Cartesian mesh size was 2.5 mm. Mesh refinement (half of the global grid size) was applied to cell layers near surfaces to keep the small-scale features, which would otherwise be filtered out during the small feature deactivation process. The spark event activated the chemistry solver, which was applied independently of the fluid cells in the computational domain. Up to 253,000 and 230,000 computational cells were used for flow and chemistry calculations, with their number depending on the operating condition and gas composition. While a grid-convergence test indicated that the grid size would affect predicted results at this level of discretization, a finer grid would have been too computationally-expensive for the number of operating conditions and NG compositions investigated here. However, a proper choice of tuning parameters

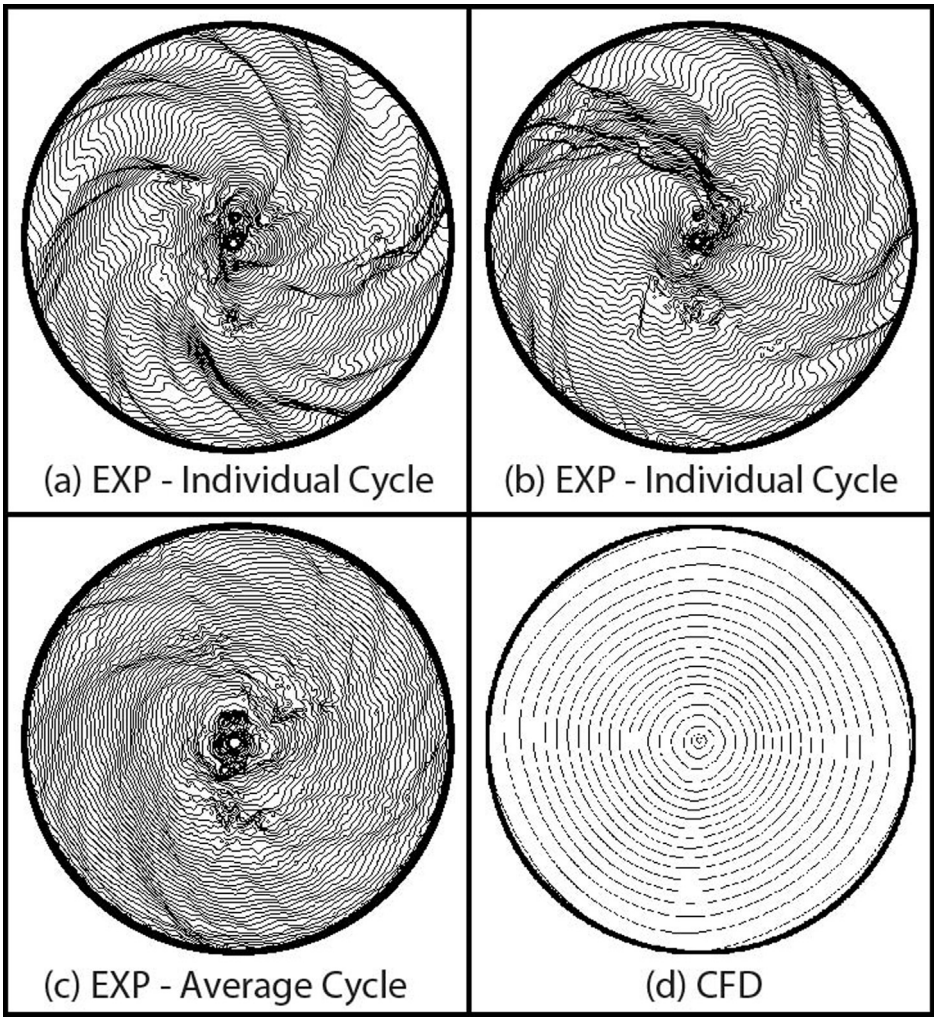

Fig. 5. Flame front propagation for (a, b) two individual cycles in the optical engine, (c) average cycle in the optical engine, and (d) CFD simulation.

allowed the under-resolved model to predict engine performance and emissions over different operating conditions without the need to modify the tuning values for each set of operating conditions, as it will be shown later in the model validation section. As the k-ε model has difficulties when dealing with flows with large streamline curvatures and time-dependent characteristics, a filter is usually employed to improve the RANS simulation results. While the authors could not find any reference with respect to the filtering method used by ANSYS® Forte, filters in RANS simulations are generally directly coupled to the grid size and the magnitude of the eddy viscosity [33]. The filtering accuracy is correlated to both the filter size and the grid size [33]. As a result, the large cells discretized from the continuous domain required the use of additional filtering on the simulation output. Specifically, a Butterworth zero-phase digital filtering was applied in post-processing to predicted in-cylinder pressure, heat release rate, and turbulent flame speed and thickness.

In addition to validating the model against experimental data over a range of operating conditions, this paper investigated the model ability to predict NG composition effects on engine efficiency and emissions using five different NG blends with different methane numbers (MN; a parameter that describes the gas resistance to knock [34]). Table 3 shows the composition of these five NG blends, including the reactive hydrogen/carbon ratio (defined as the total number of hydrogen atoms divided by the number of carbon atoms contained in the hydrocarbon components of the fuel [34]). This ratio excludes carbon atoms present in the carbon dioxide (if any) in the fuel. While the optimum spark timing in the experiments was −20 CAD ATDC, the numerical investigation used a retarded timing of −10 CAD ATDC and 8% EGR for NG composition simulations. The reason was that a higher concentration of heavier hydrocarbon in the gas composition can increase knocking probability at advanced ST. Retarded ST timing and EGR would prevent knocking and meet the safety-margin design requirements [10], particularly for this work where the lack of low-temperature reaction pathways in the used NG mechanism cannot predict knocking [25]. Table 4 details the operating conditions that were used to simulate NG composition effects. The spark timing, equivalence ratio, and engine speed were swept from −30 to −10 CAD ATDC, 0.8 to 1.0, and 900 to 2100 rpm, respectively. The bold italics denote the baseline condition.

4. Results and discussion

This section discusses the model validation and its ability to predict engine performance at different operating conditions. First, the simulation results will be compared with the experimental data to investigate if the numerical model can predict in-cylinder pressure and apparent heat release rate (AHRR) without the need to modify the tuning values at each operating condition (i.e., there is a unique set that would simulate most of the engine operation) [30]. Next, predicted flame propagation will be compared with images of flame luminosity recorded in the same engine. More, the study will investigate if the model can predict the double-peak heat release observed for advanced

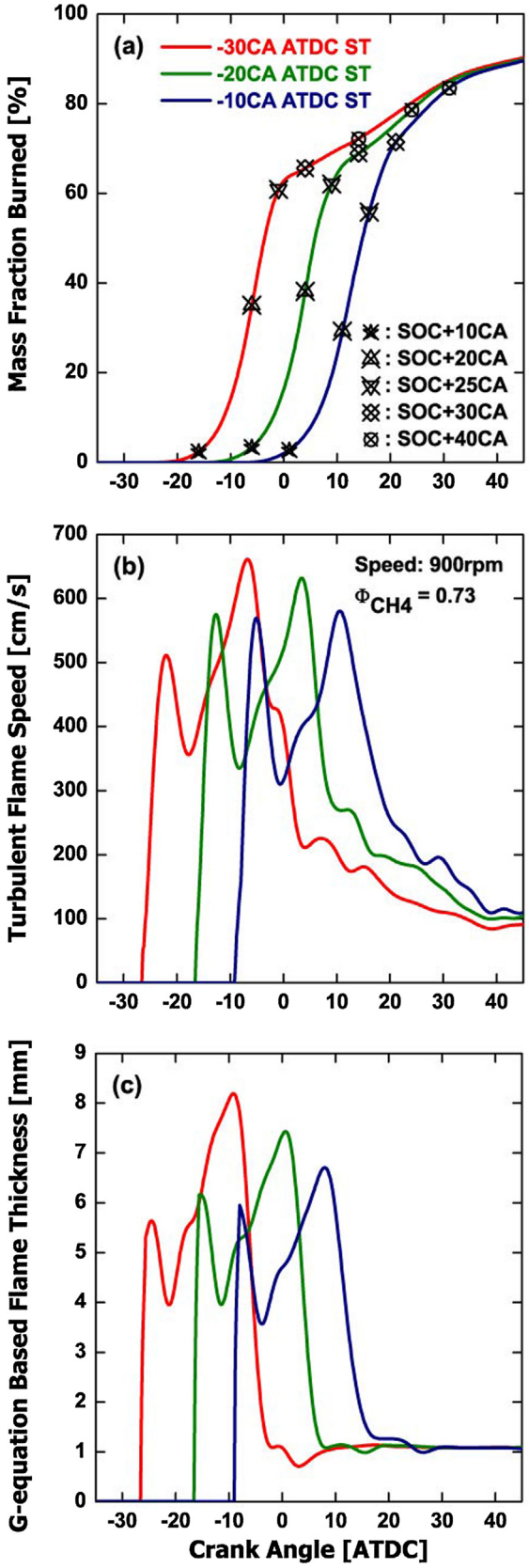

Fig. 6. Effect of spark timing on the predicted (a) mass fraction burned, (b) spatially averaged turbulent flame speed, and (c) spatially averaged G-equation-based flame thickness (CH_4, 900 rpm, $\phi = 0.73$). The markers in (a) show the mass fraction burned at several CAD of interest after SOC.

ST in the experiments (a characteristics of retrofitted CI engines that a simpler 0D or 1D SI engine models may not capture). Finally, the paper will discuss if the model can predict the NG composition effects on engine performance and emissions.

4.1. 3D CFD simulations versus experimental data

A robust engine simulation should not require extensive tuning when the operating condition or gas composition is changed. To test this hypothesis for this numerical simulation, the tuning parameters that affects the combustion model were kept constant, regardless of the simulated gas composition and/or operating condition.

The first 400 individual cycles at each operating condition were selected to validate the model. The maximum rate of pressure rise was always below 4 bar/CAD, which, together with the knock-free operation, suggests that flame propagation dominated the combustion event. More, the coefficient of variation of IMEP (COV_{IMEP}) was below 2%, which indicate a stable combustion event. Furthermore, the COV and standard deviation of peak pressure were below 8% and 4 bar, respectively. Fig. 3a shows that the simulated in-cylinder pressure and AHRR agreed well with the experimental data at the baseline condition, for both CH_4 and NG. The matched motoring section between IVC and start of combustion (SOC) validated the compression ratio, initial conditions, and boundary conditions used in the simulation. The matched section between the SOC and EVO validated the residual gas fraction and the choice of parameters used in the spark kernel model, turbulent combustion model, and other sub-models (turbulence model, wall heat transfer model, etc.). The small differences seen in Fig. 3a between the experiments and simulations can be attributed to the reduced fuel chemistry, constant boundary conditions, and submodels uncertainties. The differences during the late combustion period can be the result of neglecting the valve recesses in the model and/or by the errors in modeling the real flame behavior close to the walls.

A ST sweep using methane at 900 rpm and $\phi = 0.73$ checked if the combustion model predicted combustion behavior without the need to retune the main model parameters. Fig. 3b shows that the simulations of −30 and −20 CAD ATDC ST agreed well with the averaged experimental data except the late combustion period. The differences were probably due to the simplified in-cylinder geometry or constant boundary conditions. Fig. 4, which shows the four hundred consecutive experimental cycles at different ST, suggests that averaging the cycles can hide the late combustion. For example, several individual cycles showed a double-peak AHRR at −20 CAD ATDC ST, but not their average. This was probably due to different phasing and intensity of the second AHRR peak in individual cycles. However, Fig. 3b shows that the CFD model predicted the second AHRR peak. The CFD also captured the second AHRR peak at −30 CAD ATDC ST, but it was delayed compared to the average experimental data. Fig. 3c, which shows the data for the lower equivalence ratio cases, (0.71 vs 0.73 for CH_4 and 0.69 vs 0.71 for NG, at 900 rpm and −10 CAD ATDC ST), suggests a good agreement between CFD and experiments for both gases. Fig. 3d shows a slightly lower in-cylinder pressure for the experiments during the compression stroke when engine speed increased from 900 to 1300 rpm. This was probably due to the simulation not modeling the intake valve flow, hence not properly capturing the changes in volumetric efficiency with engine speed. Therefore, a slightly lower intake pressure was used for the initial conditions at IVC in the CFD simulations to match the experimental motoring trace.

In conclusion, the CFD model seems to reasonably predict the engine behavior at various spark timing, equivalence ratio, and engine speed, for both methane and natural gas. This suggests that the set of tuning parameters used to calibrate the model can be used to qualitatively analyze engine performance at different operating conditions and NG compositions.

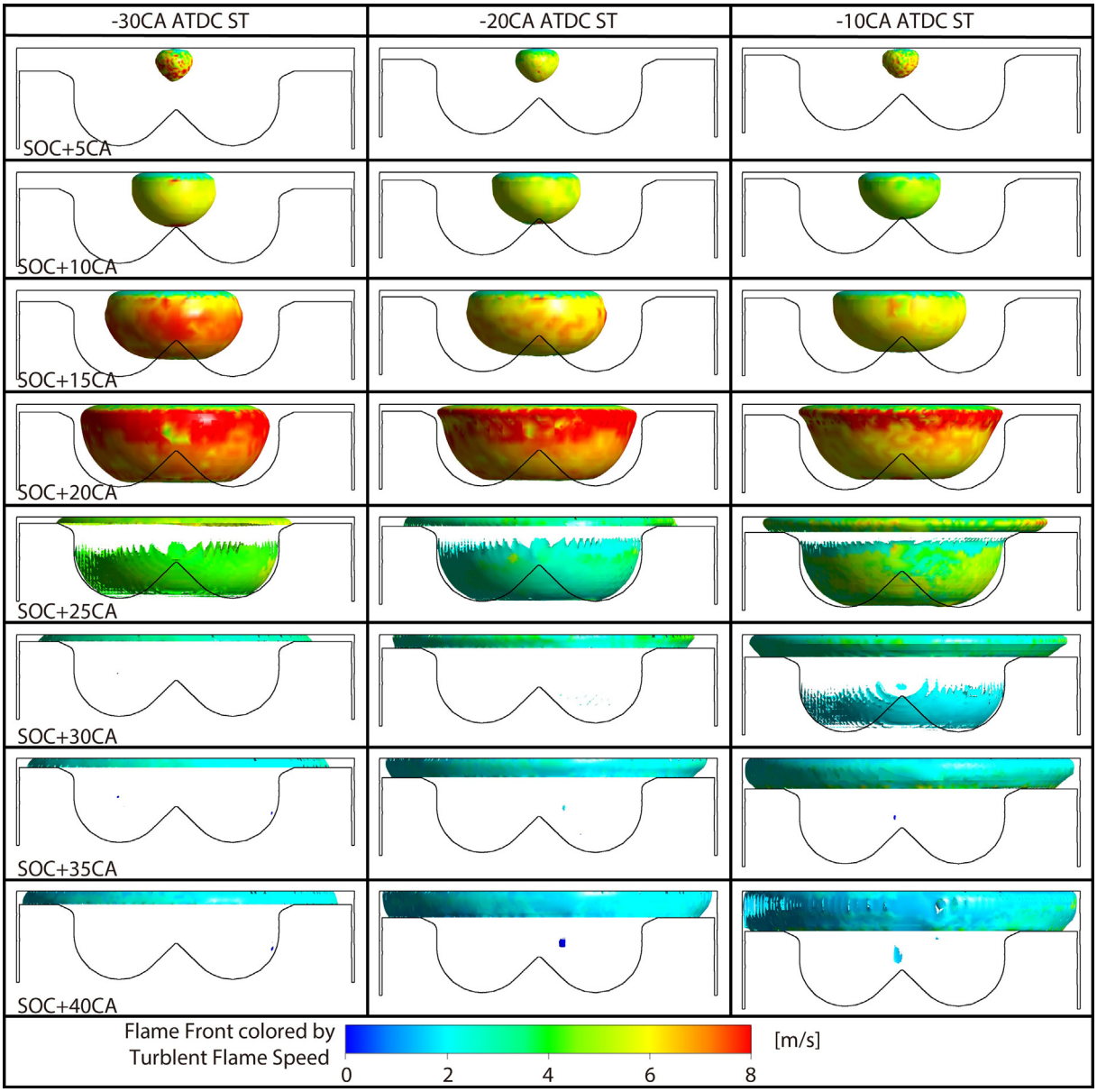

Fig. 7. Effect of spark timing on the distribution of turbulent flame speed at the flame front (i.e., G = 0) at several CAD of interest after SOC.

4.2. *In-cylinder flame propagation*

The simulated flame behavior was checked against flame images captured during an optical investigation performed in the same engine under similar operating conditions. Ref. [9] provides additional details of the optical investigation.

Fig. 5 shows the flame front propagation for both experiment and numerical simulation. Figs. 5a and b present the contours of the flame front in the flame luminosity (FL) images, which were recorded every 0.36 CAD from the spark command. Fig. 5c shows the contours of the flame front in the average FL image, also every 0.36 CAD from the spark command. Fig. 5d presents the contours of the predicted flame front every 1 CAD from the spark command, at the baseline condition. The flame front in the numerical simulation was defined as the location of $G = 0$ in the G-equation turbulent combustion model. Individual cycles showed a strong wrinkling of the turbulent flame, which was skewed towards cycles with strong flame curvature or rotation. However, the cycle-averaged flame front in the 2D images was relatively circular throughout the visualization period. Fig. 5d shows that the RANS simulation captured the flame propagation seen in the cycle-averaged flame in Fig. 5c. The counter-clockwise rotation seen in the experimental data confirms the swirl motion approach used in the CFD model. In addition, Fig. 5 validates the assumption of spherical ignition kernel in DPIK model.

Figs. 6 and 7 can provide additional insights into the double-peak heat release seen in the experiments, which this model captured. Fig. 6 shows the effect of spark timing on the predicted mass fraction burned (MFB) and the spatially averaged turbulent flame speed and thickness, for methane at baseline conditions. The markers in Fig. 6a show the MFB at several CAD of interest after SOC. The SOC in the simulation is defined as the crank angle in Fig. 6b at which the turbulent flame speed increased from zero. The turbulent flame brush thickness in Fig. 6c is defined as the square root of the Favre variance of G [25]. Fig. 7 shows the effect of spark timing on the distribution of turbulent flame speed at the flame front (i.e., at the G = 0 location), at several CAD of interest after SOC.

Figs. 6b, c, and 7 indicate a faster and thicker flame inside the bowl compared to a slower and thinner flame inside the squish region, which was probably due to differences in turbulence and heat transfer between the two regions. The main difference between the three columns

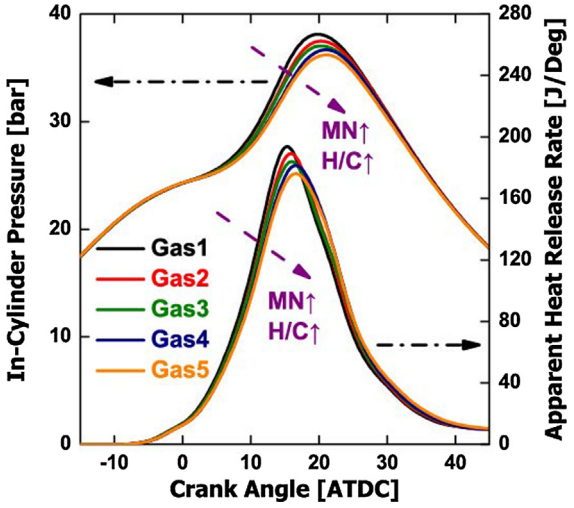

Fig. 8. Effect of NG composition on in-cylinder pressure and AHRR (baseline conditions).

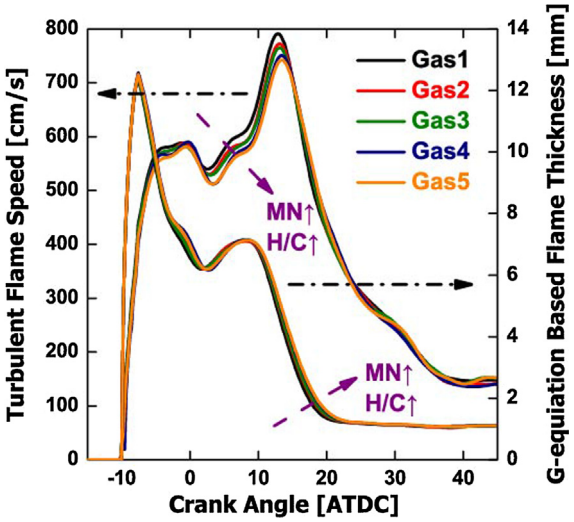

Fig. 9. Effect of NG composition on turbulent flame speed and thickness (baseline conditions).

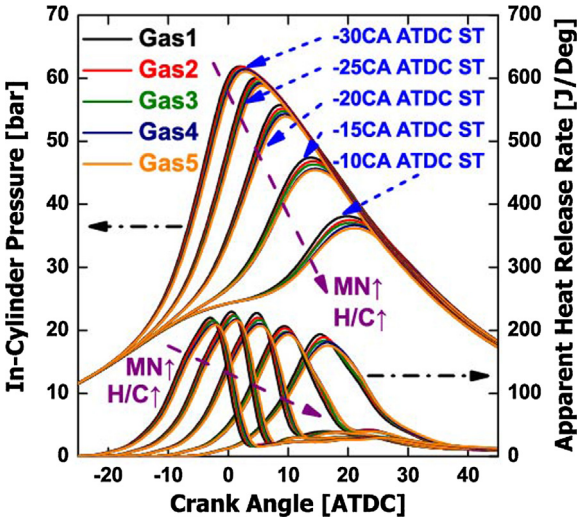

Fig. 10. Effect of NG composition and spark timing on in-cylinder pressure and AHRR.

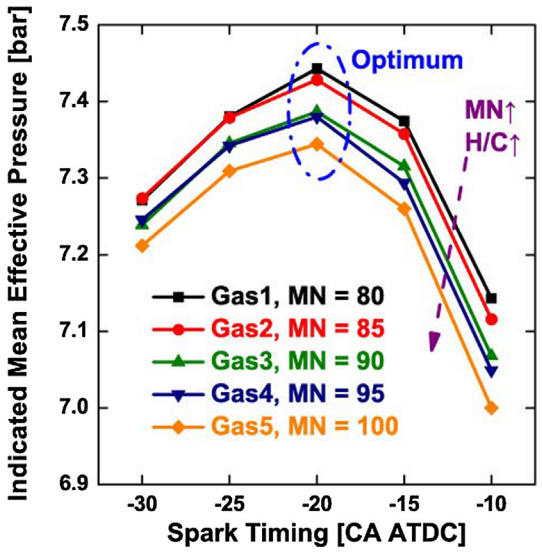

Fig. 11. Effect of NG composition and spark timing on indicated mean effective pressure.

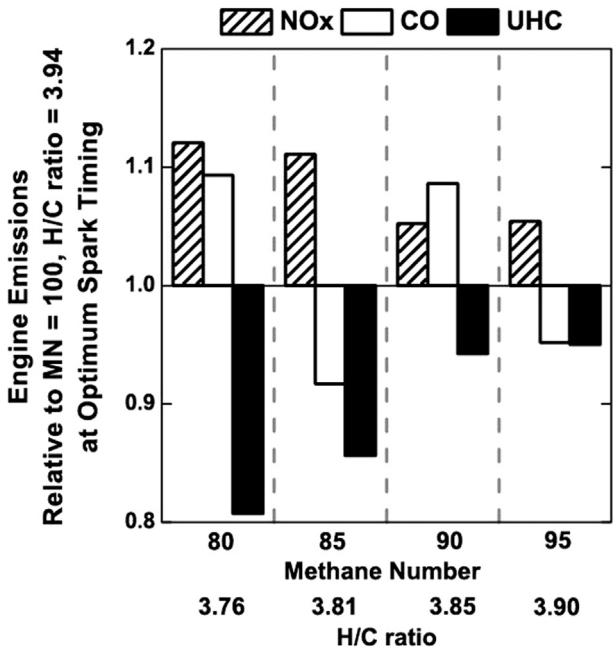

Fig. 12. Engine performance and emissions at optimum spark timing.

in Fig. 7 relates to the spark timing, while each row shows the turbulent flame speed at the flame front location after the same number of CAD after SOC. The first two rows in Fig. 7 show that, once the combustion started, the early flame development with time was similar, regardless of ST. More, Fig. 6a shows that MFBs were similar at that time. However, at SOC + 15 CAD, advanced ST increased the turbulent flame speed at the flame front, probably due to the higher turbulence inside the upward-moving bowl. At SOC + 20 CAD, when the flame arrived near the squish region entrance, just 35%, 38%, and 29% of the fuel completed the burning, for the −30, −20, and −10 CAD ATDC ST, respectively. Fig. 7 also shows that at this time, the flame front at −20 CAD ATDC ST approached the squish entrance faster than that at the more advanced ST. This can be explained by the complex interactions between the squish (including reverse squish), swirl, and combustion-induced flow. More, the flame front towards the bottom of the bowl was slower for delayed ST, probably due to flow direction changes for this case as the piston was moving rapidly downward. Then, the fuel inside

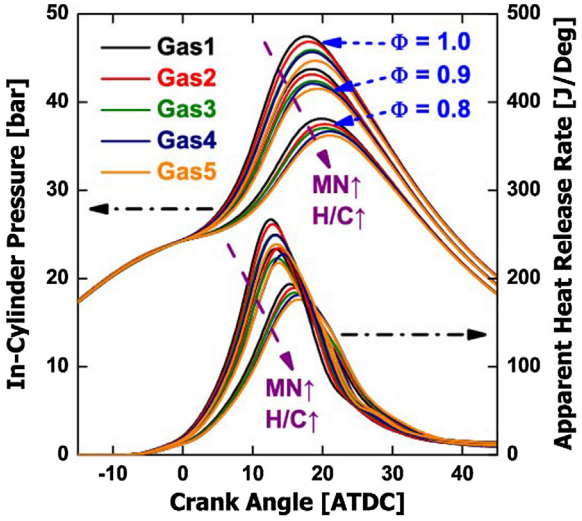

Fig. 13. Effect of NG composition and equivalence ratio on in-cylinder pressure and AHRR.

the bowl was combusted almost completely at SOC + 25 CAD. However, with just 61% and 62% MFB at −30 and −20 CAD ATDC ST, the results suggest that an important mass of fuel was trapped in the squish region at this time. In addition, Fig. 3b shows that the AHRR was around minimum for both cases. Consequently, it was this ~40% of fuel that burned in the squish region that probably produced the second AHRR peak at these two ST. The lower flame speed in Figs. 6b and 7 after SOC + 30 CAD (i.e., for the fuel in the squish region) slowed down the combustion process, which then led to similar end of combustion, regardless of ST. Fig. 7 indicates that this was due to reduced vertical spacing in the squish region, particularly for the most advanced ST. However, the data shows that ST influenced the amount of fuel remaining inside the combustion chamber after the combustion completed inside the bowl. For example, not only that most fuel burned inside the bowl at −10 CA ATDC ST but also a considerable fraction of the fuel in the squish region was also burned, as demonstrated by just 29% of the fuel remaining inside the chamber at the most retarded ST compared to 35% at the most advanced ST. More, the effect of ST on MFB increased at SOC + 40 CAD, with the highest percentage at −10 CAD ATDC ST. In addition to the the mass of fuel trapped in the squish region, one must consider the vertical spacing in the squish region when analyzing the burning speed inside the squish region. The higher vertical spacing in the squish region for retarded ST increased the local burning speed, hence the gentle decreasing slope for the AHRR. As advanced ST still had ~30% of the initial fuel mass inside the squish region, it explains why the second peak in the AHRR appeared only for advanced ST conditions (i.e., the magnitude of the late combustion was affected by the amount of fuel trapped in the squish region after the fuel inside the bowl completed its combustion).

In conclusion, for a bowl-in piston combustion chamber, the ST sweep shows that the slower, late combustion and the eventual second peak in the AHRR were due to a large fuel mass fraction inside the squish region that burned much slower compared to the inside-the-bowl combustion, at advanced ST. However, despite the lean burn operation, the flame speed was large enough to avoid flame extinction before the fuel-air mixture was completely combusted, which is one of the main concerns for lean-burn NG operation. More, it was shown that an increase in squish area can produce higher shear levels, hence an increase in the in-cylinder turbulence at the end of compression stroke, which leads to fast burning rates [35]. While more analysis is needed, this model seems capable to provide further insights into the effects of engine geometry, especially when coupled with improved kinetics. For example, the late combustion characteristics at advanced timings (that

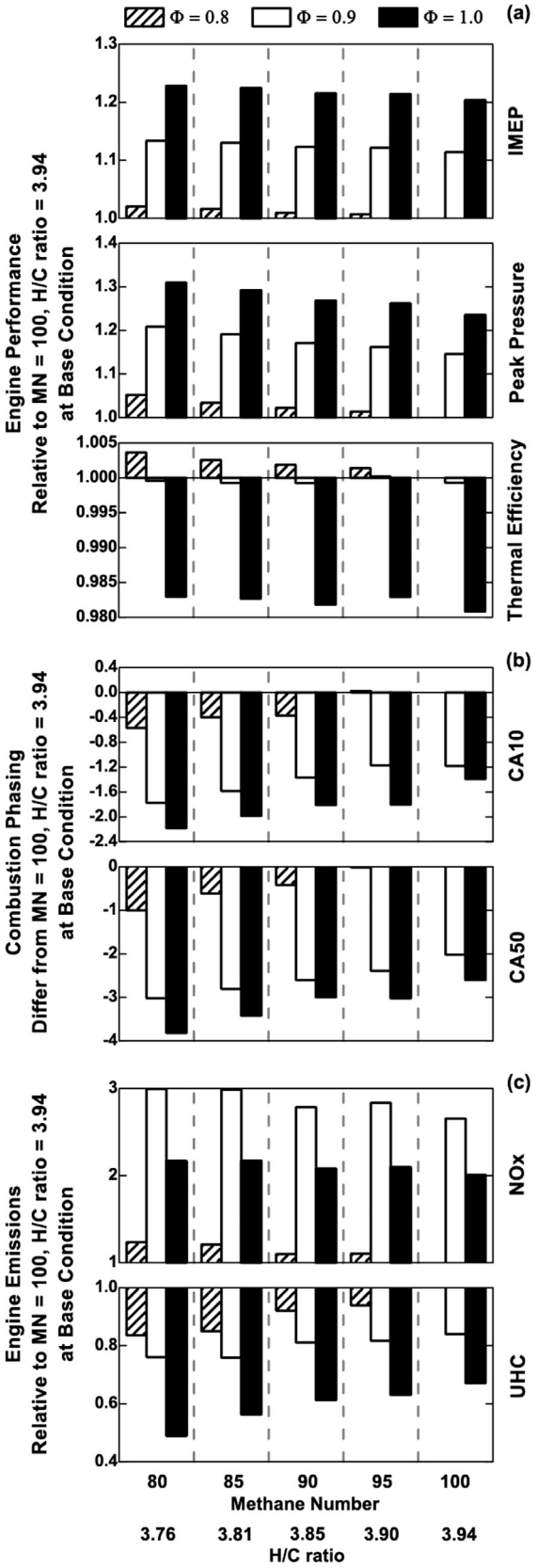

Fig. 14. Effect of NG composition and equivalence ratio on engine performance and emissions.

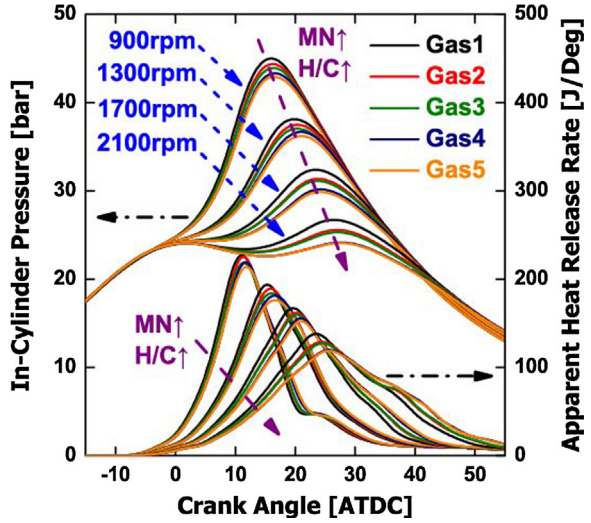

Fig. 15. Effect of NG composition and engine speed on in-cylinder pressure and AHRR.

the 3D model captured) can be used to better predict misfiring, knocking, or emissions in lean-burn NG SI applications compared to less complex 0D/1D models. The next section will show how the change in gas composition affected the prediction accuracy.

4.3. Model predictive performance

An objective for the 3D model presented here was to qualitatively predict NG composition effects at various operating conditions. This subsection discusses how model predictions compare to the literature, for the NG compositions and operating conditions shown in Tables 3 and 4.

Fig. 8 shows the pressure traces and AHRRs for the five different NG compositions, at the baseline condition. The maximum rate of pressure rise was always below 1.4 bar/CAD, regardless of fuel composition. A lower MN accelerated the heat release rate, which explains the higher and more advanced peak pressure. As less energy is needed to break a C—C bond compared to a H—C bond [3], this was probably due to the higher percentage of larger hydrocarbons for the lower MN gas. More, Fig. 9 shows that a lower MN increased the turbulent flame speed, which explains the faster heat release in Fig. 8. The gas composition had little effect on the flame thickness during the main combustion period. However, a higher MN slightly increased flame thickness during the late combustion period. Overall, NG composition affected the engine performance at the baseline condition. However, the differences were small when considering the expected cycle-to-cycle variation in a real engine, which is similar to the conclusion of Khalil et al. [36].

A ST sweep from −30 to −10 CAD ATDC was performed to find the optimal ignition timing. Fig. 10 shows that delayed ST increased the differences between these gases. However, a lower MN gas had always a higher and more advanced peak pressure, which is similar to the results of the GT-Power-based 1D-model in Ref. [37]. This was probably due to an increase in the heat transfer associated with the higher in-cylinder pressure for lower MN gases. In addition, a more advanced heat release for a lower MN gas suggests a faster flame propagation. However, the small differences between gases suggest that this engine environment can accommodate wide variations in natural gas composition, which is analog to observations made in Refs. [38,39]. Further, Fig. 11 shows that Gas 1 and 2, and Gas 3 and 4 produced similar engine performances, especially for advanced ST cases. The optimum ST for all five NG compositions was −20 CAD ATDC. At optimum ST, a lower MN improved engine performance. The trend was similar at delayed spark timing, which validated the choice of −10 CAD ATDC ST for the simulations investigating the effects of equivalence ratio and engine speed.

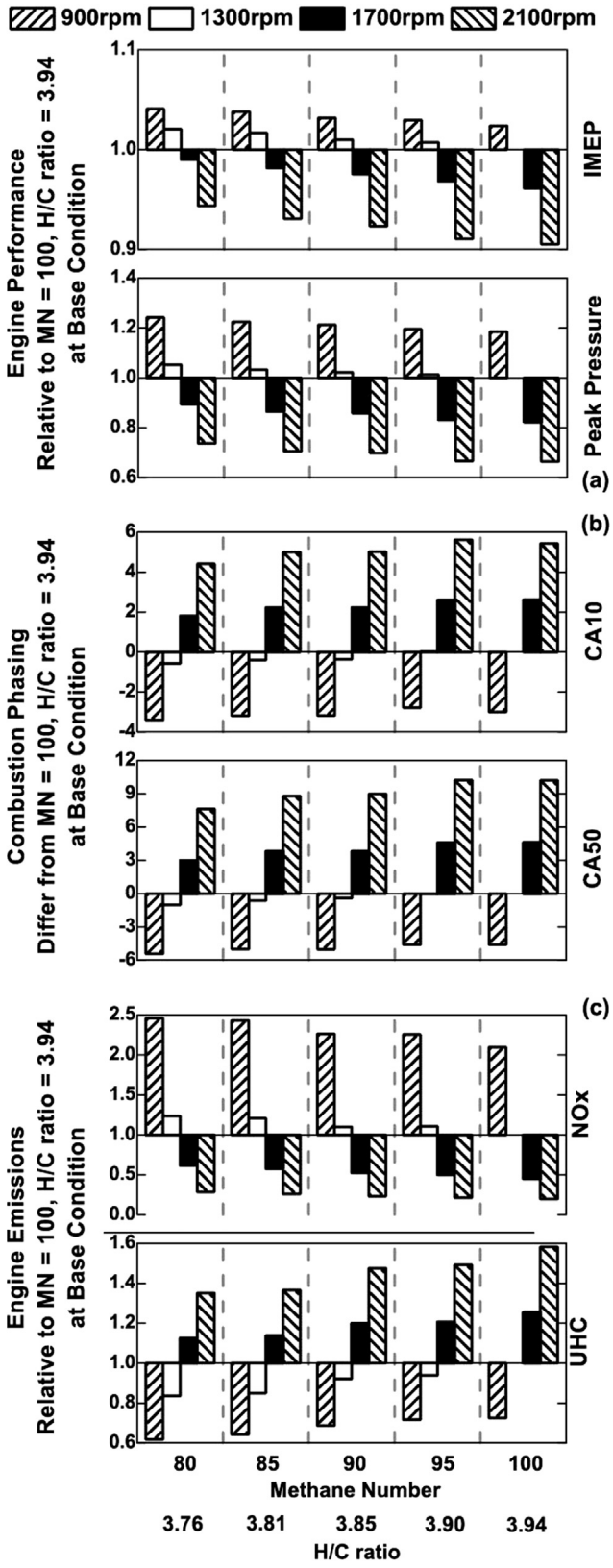

Fig. 16. Effect of NG composition and engine speed on engine performance and emissions.

While the differences in pressure or AHRR between gases were small, Fig. 12 shows that was not the case for the differences in

emissions. For example, similar to Ref. [40], NO_x emissions increased by more than 10% when MN decreased from 100 to 80, due to the corresponding increase in the bulk in-cylinder temperature. More, a lower MN decreased UHC emissions, probably due to a combination of faster flame propagation and higher bulk temperature. In addition, the simulation predicted that a lower MN will increase in CO production during the combustion process, which was similar to the observations in Ref. [40]. However, the CO emissions at the EVO showed no clear correlation with MN, which is similar to the experimental results shown in Ref. [41]. This suggests a different CO oxidation processes during late expansion, probably due to changes in the local oxygen availability. As a result, the CO emissions at EVO will not be presented in the next sections.

The model's predictive ability was also investigated for different equivalence ratios, from lean ($\phi = 0.8$) to stoichiometric ($\phi = 1.0$). Fig. 13 shows that a higher equivalence ratio increased the differences between gases, which is analog to measurements made in a stoichiometric 2007 model year Cummins ISL G [41]. Again, a lower MN gas had a higher and more advanced peak pressure compared to a high MN gas, regardless of ϕ. As expected, the AHRR showed slower flame propagation at lower ϕ, which can be explained by the decrease in flame speed for leaner mixtures.

Fig. 14a shows that a lower H/C ratio increased IMEP and peak pressure, regardless of the equivalence ratio. This is comparable to the results in dual-fuel engines, where a larger fraction of higher hydrocarbons in the NG composition improved performance [42]. Fig. 14a also shows that thermal efficiency increased with decreasing ϕ, probably due to a reduction in the heat transfer to the boundaries. As mentioned in the Section 1, this increase in engine efficiency is a major attraction for the lean-burn NG engines. However, Fig. 14a suggests that ϕ affected the differences in efficiency between the NG compositions investigated here. For example, a lower MN increased thermal efficiency at $\phi = 0.8$. But there was no clear effect of MN on efficiency for $\phi = 0.9$ and $\phi = 1.0$. Fig. 14b indicates that a lower MN advanced CA10 and CA50, probably due to the advanced flame inception. Therefore, it is possible that the less clear effect of NG composition at $\phi = 0.9$ and $\phi = 1.0$ was probably due to a higher heat transfer, which cancelled the improvements in combustion at these conditions. With respect to emissions, a low MN generally increased NO_x but lowered UHC emissions, analog to the results presented in Ref. [41]. The increase in NO_x emissions at low MN was probably due to the increase in the adiabatic flame temperature and higher burning rates [40].

To investigate the effect of engine speed on the numerical results, the engine speed was swept from 900 rpm to 2100 rpm, in 400 rpm increments, at constant equivalence ratio and spark timing. While in real engines the engine controller advances the spark timing at higher engine speeds, this study chose a constant ST to reduce the computational expense. As a result, even though Fig. 15 shows that the higher speed retarded the combustion phasing, it should not affect the qualitative effects of NG composition.[1] Fig. 15 shows that despite the MN affecting in-cylinder pressure and AHRR at all investigated engine speeds, a higher speed did not have a large effect on the differences between Gas 2 and Gas 3 or between Gas 4 and Gas 5. However, it is important to mention that the cycle-to-cycle variation can hide the difference in NG composition [7]. This is similar to Ref. [20], which mentioned that early combustion stages were more sensitive to the ignition source characteristics and flow motion around the spark plug than to large changes in gas composition.

Fig. 16 shows that a lower MN advanced CA10 and CA50 at all engine speeds, which suggests no speed effect on flame inception. More, higher MN would lower NO_x but increase UHC emissions, regardless of the engine speed. In addition, for the same gas, higher engine speed would lower NO_x but increase UHC emissions. This was probably due to the reduction in the time available to complete the chemical reactions having a larger effect on emissions than the increase in the turbulent flame speed at higher engine speeds.

[1] Several CFD simulations at higher engine speed and more advanced combustion phasing were run to check this assumption. The results show the same trend of emissions with MN, only their magnitude being slightly affected by the advanced phasing.

5. Summary and conclusions

An economical approach to convert conventional diesel engines to NG operation involves replacing the fuel injector with a spark plug and fumigating NG inside the intake manifold using a low-pressure gas injector. More, compared to conventional SI engines (i.e., roof-type head combustion chamber), these engines can run leaner, which increase their efficiency and reduce engine-out emissions. This paper presents the results of a 3D IC engine simulation using a simplified combustion model (G-equation), which can be used to analyze flame behavior and NG composition effects over a range of operating conditions. The major conclusions of this study were:

- The G-equation-based RANS simulation predicted the effects of NG composition and operating condition using a unique set of model tuning parameters, for the range of investigated spark timing, equivalence ratio, and engine speed.
- The model captured the double-peak heat release rate seen in the experiments with advanced spark timing, which is not usually captured with 0D/1D engine models.
- The predicted trends in performance and emissions were in agreement with the experiments. Lower MN increased peak pressure and IMEP. Higher H/C ratio advanced CA10 and CA50. More, a higher MN lowered NO_x but increased UHC emissions. However, while a lower MN increased CO production during the combustion process, there was no clear trend for engine-out CO emissions.

Overall, the predicted NG composition effects on engine efficiency and emissions were relatively small, at least for the range of operating conditions investigated here. However, the results suggest that the 3D CFD model described here is suitable for combustion phenomena analysis such the flame behavior inside a bowl-in-piston combustion chamber.

Acknowledgment

This material is based upon work funded by WVU and WV Higher Education Policy Commission Award #1007604R. The research was conducted at the WVU's Advanced Combustion Laboratory in Morgantown, WV. The authors gratefully acknowledge the support of ANSYS®/Reaction Design® to this research. The simulations were performed on the Super Computing System (Mountaineer) at WVU, which is funded in part by the National Science Foundation EPSCoR Research Infrastructure Improvement Cooperative Agreement #1003907, the state of West Virginia (WVEPSCoR via the Higher Education Policy Commission) and WVU. The authors gratefully acknowledge the support from WVU's CAFEE and MAE department for their assistance with comprehensive mechanical, electronic, and data-acquisition hardware/software systems, respectively.

References

[1] Liu J, Dumitrescu CE. Combustion visualization in a single-cylinder heavy-duty ci engine converted to natural gas SI operation. In: Proc. Eastern States Section of the Combustion Institute's Spring Technical Meeting, March 4–7, 2018. State College, PA, US; 2018.
[2] Reyes M, Tinaut FV, Gimenez B, Perez A. Characterization of cycle-to-cycle variations in a natural gas spark ignition engine. Fuel 2014;140:752–61.
[3] Bommisetty H, Liu J, Kooragayala R, Dumitrescu C. Fuel composition effects in a CI engine converted to SI natural gas operation. SAE Technical Paper; 2018: 2018-01-1137.
[4] Kakaee A-H, Paykani A, Ghajar M. The influence of fuel composition on the

combustion and emission characteristics of natural gas fueled engines. Renew Sustain Energy Rev 2014;38:64–78.
[5] Gupta M, Bell S, Tillman S. An investigation of lean combustion in a natural gas-fueled spark-ignited engine. J Energy Res Technol 1996;118(2):145–51.
[6] Bell SR, Loper GA, Gupta M. Combustion characteristics of a natural gas fueled spark ignited engine. Energy-sources technology conference and exhibition, January 31, 1993 – February 4. Houston, TX, USA: ASME; 1993. p. 1–9.
[7] McTaggart-Cowan GP, Reynolds CCO, Bushe WK. Natural gas fuelling for heavy-duty on-road use: current trends and future direction. Int J Environ Stud 2006;63(4):421–40.
[8] Eghbali B. Natural gas as a vehicular fuel. SAE Technical Paper; 1984: 841159.
[9] Dumitrescu CE, Padmanaban V, Liu J. An experimental investigation of early flame development in an optical SI engine fueled with natural gas. J Eng Gas Turbines Power 2018. http://dx.doi.org/10.1115/1.4039616. GTP-18-1079.
[10] Heywood JB. Internal combustion engine fundamentals. New York: McGraw-Hill; 1988.
[11] Zheng J, Huang Z, Wang J, Wang B, Ning D, Zhang Y. Effect of compression ratio on cycle-by-cycle variations in a natural gas direct injection engine. Energy Fuels 2009;23(11):5357–66.
[12] Korakianitis T, Namasivayam AM, Crookes RJ. Natural-gas fueled spark-ignition (SI) and compression-ignition (CI) engine performance and emissions. Prog Energy Combust Sci 2011;37(1):89–112.
[13] Van Der Weide J, Seppen JJ, Van Ling JAN, Dekker HJ. Experiences with CNG and LPG operated heavy duty vehicles with emphasis on US HD diesel emission standards. SAE Technical Paper; 1988: 881657.
[14] Shiells W, Garcia P. Experience with the operation of heavy vehicle engines dedicated to the use of CNG and LPG fuels. In: First International Conference and Exhibition on Natural Gas Vehicles. Sydney, Australia; 1988.
[15] Donateo T, Risi A, Laforgia D. On the computer-aided conversion of a diesel engine to CNG-dedicated or dual fuel combustion regime. In: Proc. ASME 2012 Internal Combustion Engine Division Spring Technical Conference, May 6–9, 2012, Torino, Piemonte, Italy; 2012. p. 933–43.
[16] Donateo T, Tornese F, Laforgia D. Computer-aided conversion of an engine from diesel to methane. Appl Energy 2013;108:8–23.
[17] Jiao Y, Zhang H, Yang Z, Zhang Z, Si P. Multi-dimensional simulation of combustion process in ignition nature gas engine. J Therm Sci Technol 2008;7(4):360–6.
[18] Yin Y, Liu S, Tian Y. Numerical simulation for the combustion process of spark ignition CNG engine. Internal Combus Engine Powerplant 2010;3:008.
[19] McTaggart-Cowan GP, Rogak SN, Munshi SR, Hill PG, Bushe WK. The influence of fuel composition on a heavy-duty, natural-gas direct-injection engine. Fuel 2010;89(3):752–9.
[20] Yossefi D, Belmont MR, Ashcroft SJ, Maskell SJ. Comparison of the relative effects of fuel composition and ignition energy on the early stages of combustion in a natural gas spark ignition engine using simulation. Proc Instit Mech Eng Part D: J Automob Eng 2000;214(4):383–93.
[21] ANSYS® Forte. User guide. Ansys, Inc; Release 17.2.
[22] Fan L, Li G, Han Z, Reitz RD. Modeling fuel preparation and stratified combustion in a gasoline direct injection engine. SAE Technical Paper; 1999: 1999-01-0175.
[23] Tan Z, Reitz RD. An ignition and combustion model based on the level-set method for spark ignition engine multidimensional modeling. Combust Flame 2006;145(1–2):1–15.
[24] Tan Z. Multi-dimensional modeling of ignition and combustion in premixed and DIS/CI (direct injection spark/compression ignition) engines [PhD Thesis]. University of Wisconsin–Madison; 2003.
[25] ANSYS® Forte. Forte theory. Ansys, Inc; Release 17.2.
[26] Peters N. Turbulent combustion. Cambridge University Press; 2000.
[27] Liu J, Szybist J, Dumitrescu C. Choice of tuning parameters on 3D IC engine simulations using G-equation. SAE Technical Paper; 2018: 2018-01-0183.
[28] Han Z, Reitz RD. Turbulence modeling of internal combustion engines using RNG κ-ε models. Combust Sci Technol 1995;106(4–6):267–95.
[29] Yakhot V, Orszag SA. Renormalization group analysis of turbulence. I. Basic theory. J Sci Comput 1986;1(1):3–51.
[30] Verma I, Bish E, Kuntz M, Meeks E, Puduppakkam K, Naik C, Liang L. CFD Modeling of Spark Ignited Gasoline Engines-Part 1: Modeling the Engine under Motored and Premixed-Charge Combustion Mode. SAE Technical Paper; 2016: 2016-01-0591.
[31] Verma I, Bish E, Kuntz M, Meeks E, Puduppakkam K, Naik C, et al. CFD modeling of spark ignited gasoline engines – Part 2: modeling the engine in direct injection mode along with spray validation. SAE Technical Paper; 2016: 2016-01-0579.
[32] Wahiduzzaman S, Ferguson CR. Convective heat transfer from a decaying swirling flow within a cylinder. In: 8th International Heat Transfer Conference, August 1986; 1986.
[33] Johansen ST, Wu J, Shyy W. Filter-based unsteady RANS computations. Int J Heat Fluid Flow 2004;25(1):10–21.
[34] Kubesh J, King SR, Liss WE. Effect of gas composition on octane number of natural gas fuels. SAE Technical Paper; 1992: 922359.
[35] Cho HM, He B-Q. Spark ignition natural gas engines – a review. Energy Convers Manage 2007;48(2):608–18.
[36] Khalil EB, Karim GA. A kinetic investigation of the role of changes in the composition of natural gas in engine applications. J Eng Gas Turbines Power 2002;124(2):404–11.
[37] Kim K, Kim H, Kim B, Lee K, Lee K. Effect of natural gas composition on the performance of a CNG engine. Oil Gas Sci Technol 2009;64(2):199–206.
[38] Ly H. Effects of natural gas composition variations on the operation, performance and exhaust emissions of natural gas-powered vehicles. NGV 2002 Conference Paper-Effects of Gas Composition-Aug. 2002.
[39] McTaggart-Cowan G, Huang J, Munshi S. Impacts and mitigation of varying fuel composition in a natural gas heavy-duty engine. SAE Int J Engines 2017;10(4).
[40] Kreutzer CJ, Olsen DB, Bremmer RJ. Evaluation of a lean-burn natural gas engine operating on variable methane number fuel. In: Proc. ASME 2011 Internal Combustion Engine Division Fall Technical Conference, ICEF 2011, October 2–5, 2011, Morgantown, WV, US 2011:159–166.
[41] Feist MD, Landau M, Harte E. The effect of fuel composition on performance and emissions of a variety of natural gas engines. SAE Int J Fuels Lubr 2010;3(2):100–17.
[42] Mikulski M, Wierzbicki S. Numerical investigation of the impact of gas composition on the combustion process in a dual-fuel compression-ignition engine. J Nat Gas Sci Eng 2016;31:525–37.